



Effect of Shear Direction Change on Shear-Flow-Transport Processes in Single Rough-Walled Rock Fractures

Richeng Liu^{1,4} · Na Huang^{2,3} · Yujing Jiang⁴ · Guansheng Han¹ · Hongwen Jing¹

Received: 11 September 2019 / Accepted: 29 May 2020 / Published online: 6 June 2020
© Springer Nature B.V. 2020

Abstract

Understanding the shear-flow-transport processes in rock fractures is one of major concerns for many geo-engineering practices, yet the effect of shear direction change on the flow and transport properties through rough-walled rock fractures has received little attention. In this study, a series of shear tests on artificial fractures with different surface roughness are conducted, in which the shear direction is altered perpendicularly. The distribution of apertures and its evolution during shearing are evaluated, which are further applied to simulate fluid flow and solute transport through fractures in the directions parallel and perpendicular to shear direction using a finite element method code. The effect of shear direction change on flow and transport properties of rock fractures is systematically investigated. The results show that when the shear direction is changed perpendicularly during shearing, the normal displacement changes from increasing (i.e., dilation) to decreasing (i.e., closure) with increasing shear displacement. The final normal displacement depends on the competition between dilation and closure induced by the shear in two directions, which directly determines the aperture distribution thereby affecting the flow and transport processes through fractures. The closure is more significant for the fracture with a smaller JRC, resulting in a more dramatic decrease in equivalent permeability. The historical shear stress can either promote or block the solute transport depending on the distributions of void spaces and contact obstacles induced by shearing in two perpendicular directions. The Peclet number decreases during shearing in spite of the magnitude of historical shear displacement, indicating that the dispersion becomes much significant with shearing due to the increasingly concentrated contact areas and flow channels.

Keywords Rock fracture · Shear direction change · Fluid flow · Solute transport · Shear displacement

✉ Na Huang
huangna@upc.edu.cn

¹ State Key Laboratory for Geomechanics and Deep Underground Engineering, China University of Mining and Technology, Xuzhou 221116, People's Republic of China

² Key Laboratory of Unconventional Oil & Gas Development (China University of Petroleum (East China)), Ministry of Education, Qingdao 266580, People's Republic of China

³ School of Petroleum Engineering, China University of Petroleum (East China), Qingdao 266580, Shandong, China

⁴ School of Engineering, Nagasaki University, 1-14 Bunkyo-machi, Nagasaki 8528521, Japan

1 Introduction

In fractured rock masses with low matrix permeability, the rock fractures provide main pathways for the flow of fluids and transport of dissolved solutes. Understanding how the flow and transport characteristics within fractures evolve with space and time is of crucial importance in many practical applications, including groundwater contamination and remediation, geothermal energy extraction, underground gas/oil storage and disposal of radioactive waste (Neretnieks 1980; Barbier 2002; Sun and Zhao 2010). The fluid flow and solute transport in rock fractures are significantly dependent on the geometry of void spaces (i.e., aperture) between two walls of a fracture. The fracture aperture varies sensitively according to the mechanical loading conditions (Lanaro 2000; Rahman et al. 2002; Li and Sun 2019), indicating that the flow and transport characteristics are coupled to the mechanical behavior of rock fractures. The engineering practices have demonstrated that the fractured rock masses may experience different loading histories both in the magnitude and orientation with respect to the rock fracture (Hudson 1990; Zhang et al. 2001). According to different loading histories, the rock fractures are subjected to different normal and shear stresses, in which the shear direction may change arbitrarily. Both the magnitude and direction of shear stress affect the magnitude of apertures, thereby determining the flow and transport behaviors through rock fractures.

The shear-flow characteristics of rock fractures are influenced by various factors, including normal stress (Li et al. 2008; Watanabe et al. 2009; Javadi et al. 2014; Rong et al. 2016; Zhou et al. 2018; Huang et al. 2019), surface roughness (Brown et al. 1987; Thompson and Brown 1991; Boutt et al. 2006; Auradou et al. 2006; Crandall et al. 2010; Zou et al. 2015; Wang et al. 2016; Huang et al. 2017), scale effect (Tsang and Witherspoon 1983; Raven et al. 1985; Fardin 2003; Matsuki et al. 2006; Koyama et al. 2006; Huang et al. 2018), and shear direction (Entire et al. 1997; Matsuki et al. 2010; Cheng et al. 2017; Liu et al. 2018a, b). The results show that the permeability of fractures decreases with the increment of normal stress due to fracture closures. On the contrary, the fracture aperture increases/dilates as shear advances, thereby increasing the permeability of fractures. The change in flow field due to stress affects the transport behavior through rock fractures. Vilarrasa et al. (2011) investigated the effect of coupled shear-flow process on solute transport in rough-walled rock fractures. They found that shear-induced channels yield an advection-dominated transport behavior in the direction parallel to shear direction and dispersion-dominated transport behavior in the direction perpendicular to shear direction. Zhao et al. (2011) confirmed that the stress not only significantly changes the solute residence time, but also alters the solute travel paths through rock fractures, highlighting the importance of coupled stress-flow-transport processes in fractured media. However, in the previous studies mentioned above, the fractures have mostly been subjected to the shear stress with a fixed shear direction.

The change of shear direction has been considered in cyclic shear loading, in which the direction of shear load is repeatedly reversed. Hutson and Dowding (1990) performed a series of cyclic shear loading tests on 30 sawn rock fractures and proposed a wear equation for estimating the fracture asperity during shearing. Lee and Cho (2002) observed somewhat irregular variation of fracture permeability during cyclic shear loading, especially after the first shear loading cycle, due to the competing interaction from dilation and production of gouge materials. Chern et al. (2012) analyzed the mechanical behavior of regular triangular fractures during cyclic shear tests and estimated the asperity degradation of fractures as a function of joint roughness, normal stress, shear displacement and number of

loading cycles. In the above studies, although the shear behaviors with repeatedly reversed shear directions have been studied, the shear direction change of 90° during shearing has not been considered. Especially when it comes to the shear-flow-transport behaviors of rock fractures, quantifying the effect of shear direction change on the flow and transport properties of fractures has not been attempted before, if any.

The main objective of this study is to analyze the effect of shear direction change on shear-flow-transport processes in single rough-walled rock fractures. The shear tests, in which the shear direction is altered perpendicularly, were conducted on two fractures with different surface roughness. The numerical simulations on fluid flow and solute transport processes in fractures during shearing were performed using a finite element method (FEM) code. Finally, the influences of shear direction change on flow and transport channels, equivalent permeability, breakthrough curves, and Peclet number were systematically investigated.

2 Experimental Setup

2.1 Fracture Specimen Preparation

The shear process on an originally well-mated fracture specimen as shown in Fig. 1a is considered, in which the lower specimen is sheared along x direction (Fig. 1b) and then sheared along y direction (Fig. 1c), while the upper specimen is fixed. The current shear test apparatuses usually move only in unidirectional and/or bidirectional (forward/reverse) paths, thus changing the shear direction with an inclination angle of 90° during shearing is almost impossible. In this study, a well-mated fracture specimen as shown in Fig. 1a is first manufactured. Then the lower part of the fracture specimen is sheared. This direction of the shear is denoted as x direction and the shear displacement is represented by u_x . Assuming that the damage of asperities during shearing is negligible, another fracture specimen with the length of $L' = L - u_x$ as shown in Fig. 1b is manufactured to represent the state of fractures after the shear displacement of u_x . We rotate the fracture specimen 90° and then conduct the shear test on this rotated fracture specimen. In this way, the shear direction is changed perpendicularly along the y direction as show in Fig. 1c. The artificial fractures, which are made of a mixture of plaster, water and retardant with a weight ratio of 1:0.2:0.005, are used in the tests so that the initial conditions can be reproduced by creating multiple replicates of the same fracture. A lot of shear tests have been done based on this material (Jiang et al. 2004a, b; Li et al.

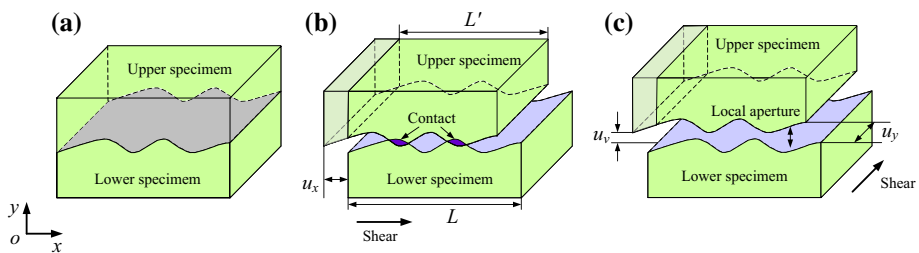
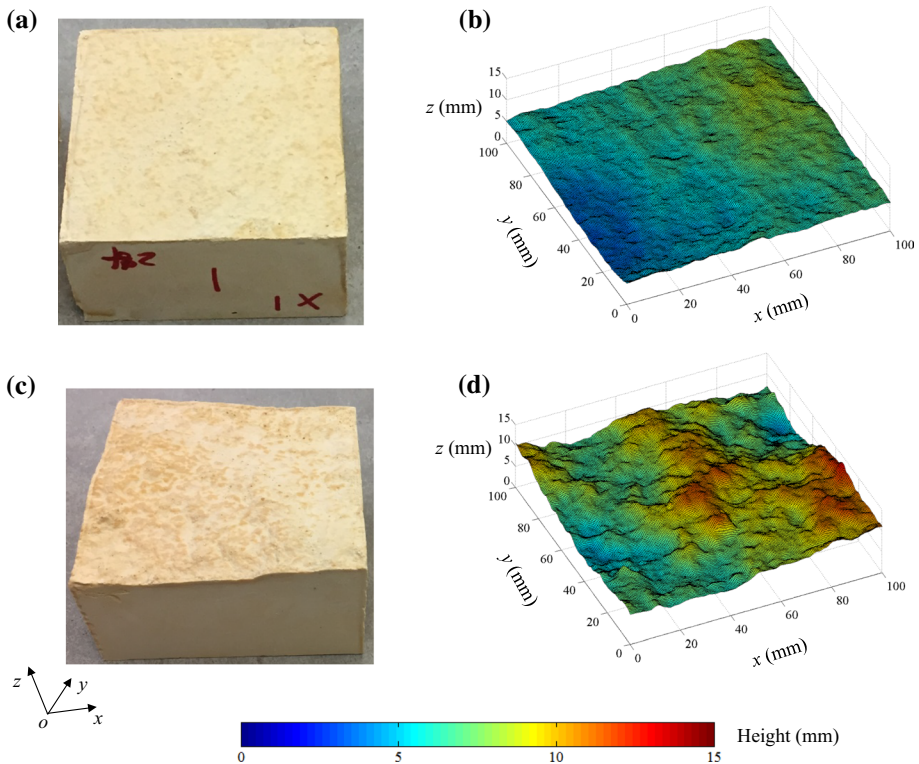


Fig. 1 Schematic diagram of change in shear directions: **a** initial state, **b** shearing in x direction and **c** shearing in y direction

Table 1 Physical properties of fracture samples

Physical properties	Variable	Value	Unit
Density	ρ	2.066	g/cm^3
JCS	σ_c	47.4	MPa
Elastic modulus	E_s	28.7	GPa
Poisson's ratio	ν	0.23	–
Tensile strength	σ_t	2.5	MPa
Cohesion	c	5.3	MPa
Basic friction angle	φ	63.3	degree

**Fig. 2** Two fracture specimens and the corresponding topographical models measured using a 3D laser scanning profilometer system: **a, b** X1 and **c, d** X2

2008). The results indicate that the artificial fractures show realistic shear behaviors. The physical properties of the samples are shown in Table 1 (Jiang et al. 2006). Two kinds of artificial fractures labeled as X1 and X2 are manufactured as shown in Fig. 2. The surfaces of the two fractures were measured using a 3D laser scanning profilometer system. The joint roughness coefficient (JRC) of X1 and X2 is calculated in both x and y directions based on the measured surface data. The JRCs of X1 in x and y directions are 3.314 and 5.982, respectively, and the JRCs of X2 in x and y directions are 11.876

and 13.271, respectively. This indicates that X2 has a rougher surface than X1 in both x and y directions. For each fracture specimen, the lengths of lower and upper blocks are 100 mm and $(100 - u_x)$ mm, respectively, in which $u_x = 0, 5, 7$ and 9 mm. When $u_x = 0$, the two blocks are well-mated. The width and height of specimens are both 100 mm.

2.2 Shear Test Apparatus and Experimental Procedure

Figure 3 shows the digital-controlled shear testing apparatus used for investigating the shear behaviors of rough-walled rock fractures. The device consists essentially of a hydraulic-servo actuator unit, an instrument package unit and a mounting shear box unit. The normal and shear forces are applied by a servo-controlled hydraulic pump with the loading capacity of 400 kN. Their magnitudes are measured by three load cells that are located at two sides of the shear box. The vertical and horizontal displacements are measured by two LVDTs (linear variation displacement transducers) that are attached to the top and side of the shear box. The shear box consists of a lower half and an upper half. During shearing, the upper box is allowed to move perpendicularly and the lower box is allowed to move horizontally. The maximum vertical and shear displacements are 10 mm and 20 mm, respectively. A series of experimental tests have been carried out using this apparatus, indicating good performances in the direct and/or cyclic shear tests (Jiang et al. 2004b; Wu et al. 2018).

The shear tests were conducted on a series of fracture specimens under a constant normal stress of 1.0 MPa. The specimens were sheared up to 10 mm in x direction and 20 mm in y direction with a rate of 0.5 mm/min. Some spacers were placed into the shear box to fix the upper fracture block whose size is smaller than that of the shear box. The height of each spacer is smaller than 50 mm to avoid contact between the spacer and the lower fracture block during shearing.

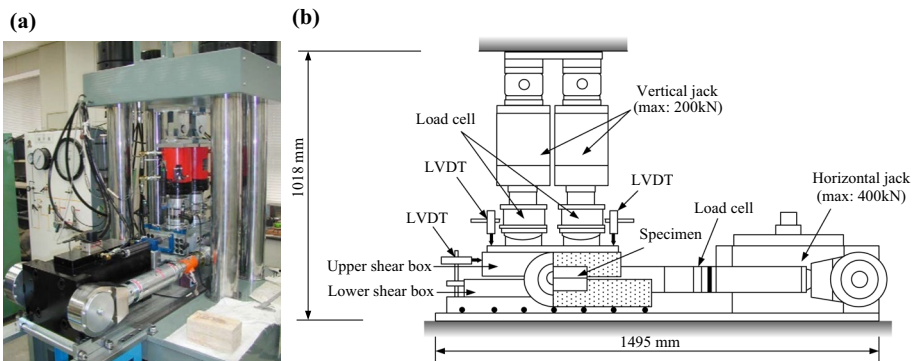


Fig. 3 Digital-controlled shear testing apparatus: **a** photograph and **b** schematic view (Jiang et al. 2004a, b)

3 Numerical Simulations

3.1 Fluid Flow in Rock Fractures

Fluid flow through a parallel plate is modeled according to the following cubic law (Witherspoon et al. 1980; Zimmerman and Bodvarsson 1996):

$$q = - \frac{w\rho g b e^3}{12\mu} \nabla h \quad (1)$$

where q is the volumetric flow rate, w is the width of a fracture, ρ is the fluid density, g is the gravitational acceleration, e is the hydraulic aperture that equals to the vertical distance between two parallel plates, μ is the dynamic viscosity, and h is the hydraulic head. However, for a natural rough-walled fracture, it is difficult to assign a unified aperture due to the irregular distribution of surface asperity. An approximation method is to divide the void spaces between the two fracture surfaces into a series of small connected parallel plates having variable apertures, which yields the following Reynolds equation (Brown et al. 1995):

$$\nabla \cdot \left(\frac{\rho g b_{ij}^3}{12\mu} \nabla h \right) = 0 \quad (2)$$

where b_{ij} is the local mechanical aperture of each simplified parallel plate. Reynolds equation is a simplified form of Navier–Stokes equation. It takes into account of aperture heterogeneity within fractures by neglecting the inertial effects of flow. When the flow velocity is low and the fracture has slowly varying aperture field, the Reynolds equation can be utilized to describe the fluid flow through rough rock fractures (Brown 1987; Koyama et al. 2008; de Dreuzy et al. 2012). The total volumetric flow rate Q through the fracture is equal to the integral of local volumetric flow rate through a section of the fracture. The equivalent permeability K of the fracture can be back-calculated according to:

$$Q = - \frac{AK\rho g}{\mu} J \quad (3)$$

where A is the cross-sectional area and J is the hydraulic gradient between the inlet and outlet boundaries.

The mechanical aperture b of a fracture is changed with normal and shear displacements, which can be estimated as:

$$b(x, y) = \begin{cases} Z(x + u_x, y) - Z(x, y) + u_v & \text{If sheared in } x \text{ direction} \\ Z(x, y + u_y) - Z(x, y) + u_v & \text{If sheared in } y \text{ direction} \end{cases} \quad (4)$$

where $Z(x, y)$ represents the asperity height of a fracture and u_v is the normal displacement that is determined based on shear tests. The negative value of local aperture in Eq. (4) represents the contacts between the two fracture walls (Brown 1987; de Dreuzy et al. 2012). At each shear interval, the previous aperture field is redistributed with some new contact points and void spaces. Thus, the aperture distribution should be re-calculated for each shear interval. Equation (4) is valid when the asperity damage was assumed to be negligible and influence of gouge material developed during shearing on the fluid flow and solute

transport is not considered in this study. The b_{ij} in Eq. (2) at different shear displacements can be determined element by element according to the evaluation results of b in Eq. (4).

Two different kinds of boundary conditions (unidirectional flows in x and y directions) are considered in this study as shown in Fig. 4. As the shear displacement increases, the effective length of the nominal contact between two fracture surfaces decreases; thus, a decreasing hydraulic head is applied on the inlet boundary while keeping a constant hydraulic gradient of 0.001 between the inlet and outlet boundaries. Other boundaries are set no flow boundaries. The density and dynamic viscosity of water at 20° are $\rho = 998.2 \text{ kg/m}^3$ and $\mu = 0.001 \text{ Pa s}$, respectively.

3.2 Solute Transport in Rock Fractures

The calculated flow fields at different shear displacements are used to predict the transport of solutes through a rough-walled fracture, which can be accomplished by directly solving the advection–dispersion equation (Bear 1972):

$$\frac{\partial c}{\partial t} = -\mathbf{V} \cdot \nabla c + \nabla \cdot (\mathbf{D}\nabla c) \tag{5}$$

where c is the solute concentration that is a dimensionless quantity normalized to the inlet concentration, t is time, \mathbf{V} is the flow velocity, the magnitude of which in each element can be estimated by:

$$\mathbf{V} = -\frac{\rho g b_{ij}^2}{12\mu} \nabla h \tag{6}$$

and D is the dispersion tensor that is a symmetric positive semi-definite tensor. The dispersion coefficient D_{ij} for each local parallel plate is defined as:

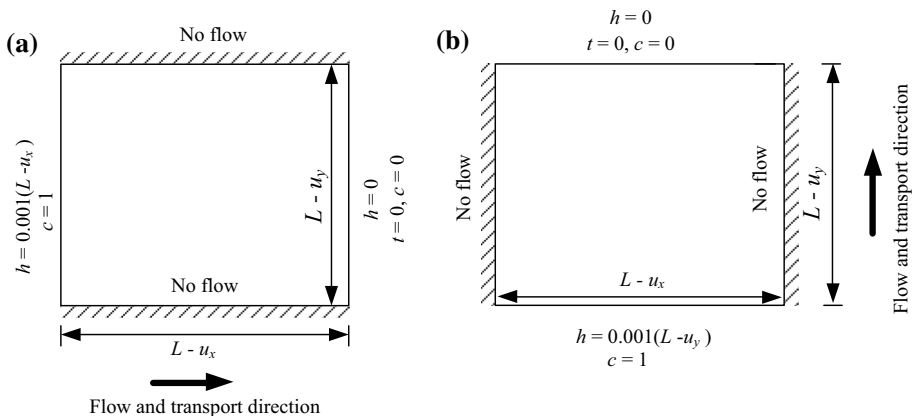


Fig. 4 Boundary conditions for two flow and transport patterns: **a** in x direction, and **b** in y direction

$$\begin{cases} D_{xx} = \frac{1}{\sqrt{v_x^2+v_y^2}}(\alpha_L v_x^2 + \alpha_T v_y^2) + D_m \\ D_{xy} = D_{yx} = \frac{1}{\sqrt{v_x^2+v_y^2}}(\alpha_L - \alpha_T)v_x v_y + D_m \\ D_{yy} = \frac{1}{\sqrt{v_x^2+v_y^2}}(\alpha_T v_x^2 + \alpha_L v_y^2) + D_m \end{cases} \tag{7}$$

where v_x and v_y are local flow velocities in the x and y directions, respectively, α_L and α_T are the longitudinal and transverse dispersivity, respectively, and D_m is the molecular diffusion coefficient. In this study, we assume a constant α_L of 0.5 cm and a constant α_T of 0.2 cm (Wang and Zhou 2004). In Eq. (5), the dispersive effect of velocity variation on solute transport is explicitly represented, whereas the effects of retardation factors such as matrix diffusion, sorption and decay on the solute transport are not taken into account. At $t=0$, the value of c at the inlet boundary is set to 1.0. The time-dependent solution of Eq. (5) describes the distribution of solute concentration within the fracture as a function of time. The average solute concentration at outlet boundary can be computed as (Thompson 1991):

$$\bar{c} = \frac{\int_0^w c(L, y)b(L, y)dy}{\int_0^w b(L, y)dy} \tag{8}$$

Note that Eq. (8) is written in the case of flow and transport in x direction. The breakthrough curve can be obtained by plotting \bar{c} versus t . Then the following analytical solution of one-dimensional advection–dispersion is used to fit the breakthrough curve (de Marsily 1986):

$$c(x, t) = \frac{1}{2} \left[\operatorname{erfc} \left(\frac{x - Ut}{2\sqrt{D_L t}} \right) + \exp \left(\frac{Ux}{D_L} \right) \operatorname{erfc} \left(\frac{x + Ut}{2\sqrt{D_L t}} \right) \right] \tag{9}$$

where U is the effective tracer velocity and D_L is the longitudinal dispersion coefficient.

Equation (9) describes the solute transport behaviors through a smooth parallel plate with a uniform flow field and no dispersion. In the application of this equation to a rough-walled fracture, D_L is used to account for the fluctuation of flow velocity. Both U and D_L are regarded as adjustable parameters to fit the breakthrough curve. The Peclet number (Pe), which compares advection with dispersion, is estimated according to:

$$Pe = \frac{UL}{D_L} \tag{10}$$

Solute transport with the overall flow in x and y directions are considered, respectively. The solute concentration in the fracture is initially set to be zero with a dimensionless concentration at inlet boundary that equals to 1.0.

The commercial FEM software COMSOL Multiphysics was utilized to sequentially solve the Reynolds equation and the advection–dispersion equation. The aperture field is divided into 1000×1000 small elements with an edge length of 0.1 mm. The flowchart to estimate the shear-flow-transport processes through single rough-walled fracture is displayed in Fig. 5. Under a constant normal stress of 1.0 MPa, the fracture specimen is sheared along x direction and then sheared along y direction. The evolution of normal displacement with shear displacement is recorded during shearing, and the data are used to calculate the aperture distribution with combination of the measured topographical data

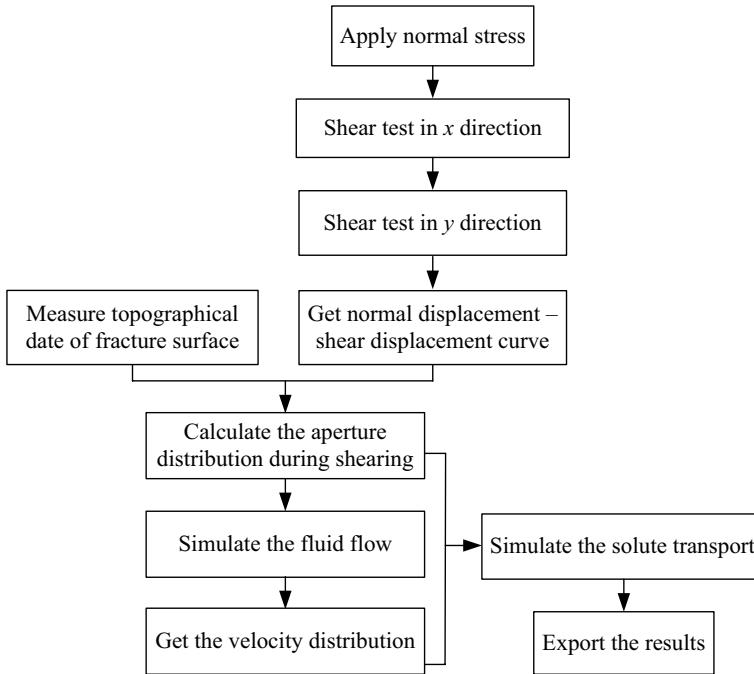


Fig. 5 Flowchart to estimate the shear-flow-transport processes through single rough-walled fracture

of fracture surface. The fluid flow through fractures during shearing is simulated by solving Eq. (2), and the local permeability of the fracture is different from element to element according to the obtained aperture distributions. The flow velocity of each element can be evaluated based on the flow simulation results, which is further used to simulate the solute transport process by solving Eq. (5).

4 Results and Analysis

4.1 Evolutions of Mechanical Behaviors During Shearing

The shear behaviors of fracture specimens X1 and X2 are illustrated in Fig. 6. Figure 6a, b shows the evolutions of shear stress and normal displacement with shear displacement in x direction, respectively. As shown in Fig. 6a, the shear stress τ increases rapidly to a peak strength, and then gradually decreases to a residual value that remains constant as shear displacement continues. The evolution of τ with u_x of X2 is similar to that of X1 except that the peak shear strength for X2 is larger than that for X1. The normal displacement u_v for both X1 and X2 slightly decreases to a minimum value at the beginning of shearing as indicated in Fig. 6b. As u_x continuously increases, u_v of X1 increases first and then maintains a substantially constant value, while u_v of X2 keeps increasing with a first increasing and then decreasing gradient. The u_v of X2 is larger than that of X1 at a relatively large u_x (i.e., $u_x > 6$ mm) due to a larger dilation induced by a rougher surface. The shear behaviors of X1 and X2 in y direction indicated in Fig. 6c, d are consistent with the direct shear test

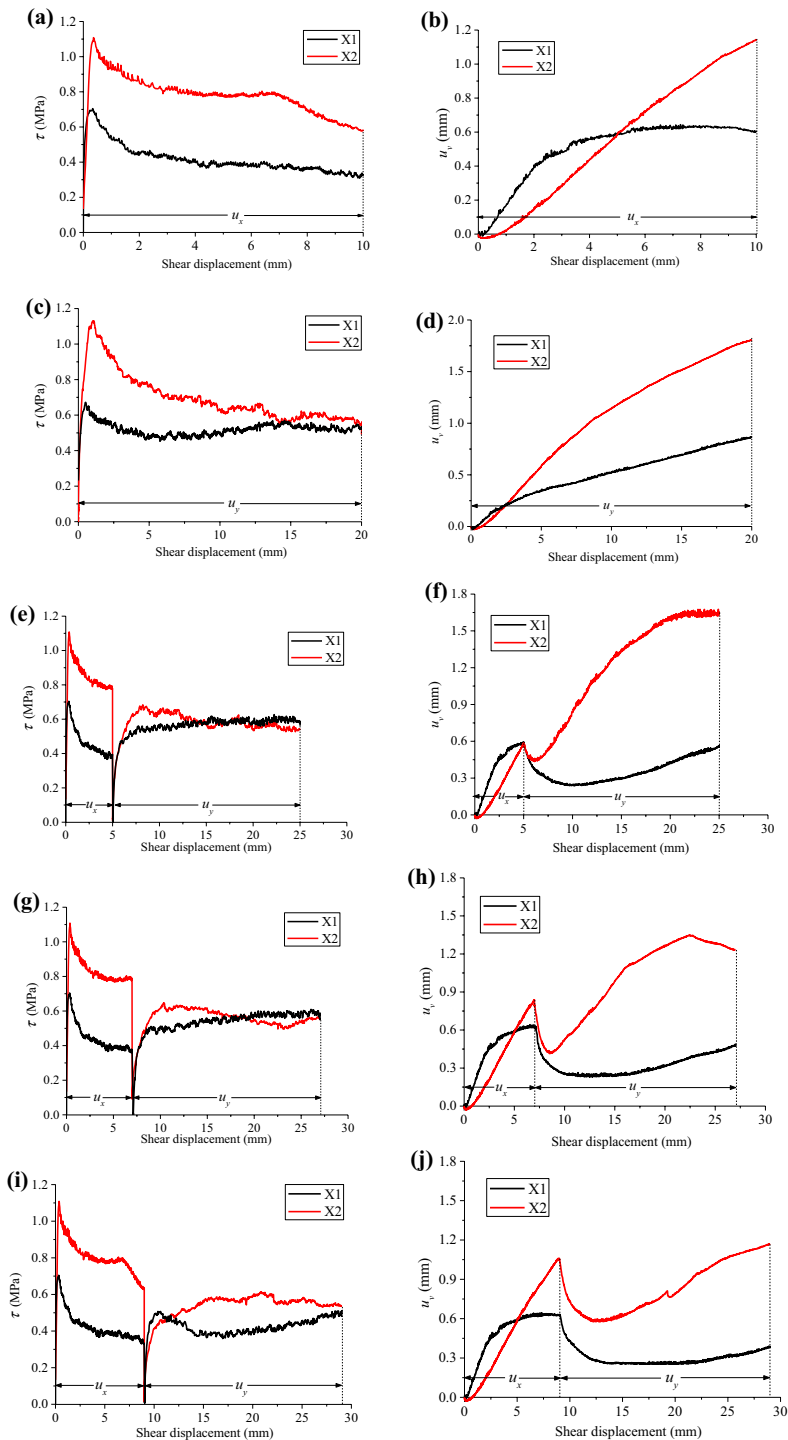


Fig. 6 Test results of specimens X1 and X2 during shearing: **a, b** direct shear in x direction, **c, d** direct shear in y direction and **e–j** shear in different combinations of x and y directions

results in x direction. These results are in good agreement with the previous observations in direct shear tests for real rock fractures (Olsson and Barton 2001; Li et al. 2008; Indraratna et al. 2015).

When there exists a historical u_x (i.e., $u_x \neq 0$) as indicated in Fig. 6e, g, i, τ directly increases to the residual value after the shear direction changes perpendicularly, in which the peak shear strength does not appear or is not obvious. The residual shear stresses are very close in spite of the magnitude of u_x . The u_y gradually decreases at the beginning of the shear in y direction as shown in Fig. 6f, h, j, indicating a continuous closure between two fracture surfaces. This is because that during shearing in x direction, asperities dipping toward x direction deform elastically and areas inclined in y direction are detached, generating void spaces in y direction. As the shear direction shifts from x to y direction, these void spaces allow further closure between two fracture surfaces. The closure increases with increasing u_x , and the increment becomes more obvious for X2 that has a larger JRC. After reaching to a minimum value, u_y changes to increase as shear displacement continues, and the gradient of increment increases first and then decreases with increasing u_x .

Figure 7 indicates the evolutions of aperture distributions under different u_x for X1 and X2. For all cases, the aperture-frequency curve changes from sharp to flat with increasing u_y , indicating an increasing mean mechanical aperture and deviation. However, this tendency is restricted with increasing u_x . As u_x increases, the front part of aperture-frequency curve moves down while the change of the tail of the curve is not obvious. Comparisons between the aperture ranges of X1 and X2 under the same u_x and u_y show that a fracture with a larger JRC tends to generate a wider range of aperture distributions. Figure 8a–h displays the evolutions of contact areas with u_x for X1 and X2 when the shear displacement in y direction is fixed to be 9 mm. For both X1 and X2, plenty of small contact areas are dispersedly distributed within the fracture under a small historical shear displacement u_x . As u_x increases, the contact areas gradually converge in a few major contact spots with increasing contact areas. The variations in contact ratio (R_c) defined as the ratio of contact area between two fracture surfaces to the area of the entire fracture plane are displayed in Fig. 7i, f, in which a larger R_c is obtained for the X1 with a smaller JRC. The R_c increases as u_x increases, indicating that the historical shear in x direction promotes the fracture closure during shearing in y direction.

4.2 Fluid Flow Properties

Figure 9 shows the aperture distributions and main flow paths in x and y directions during shearing. In the direct shear test (i.e., $u_x = 0$ mm), a large number of small void spots dispersedly distributed within the fracture plane at the beginning of shearing as shown in Fig. 9a, e, and then the number of contact spots decreases while the area of single spots increases significantly with increasing u_y , resulting in obvious flow channels in both x and y directions as shown in Fig. 9b, f. There also exist some regions with nonzero apertures that are surrounded by contact areas, and these island regions make no contribution to fluid flow. When $u_x = 9$ mm, the historical shear in x direction is prone to generate striped contacting asperities and void spaces perpendicular to the shear direction. The generated contacts block the flow in x direction (Fig. 9c, d) while the induced channels promote the flow in y direction (Fig. 9g, h). Figure 10 displays the calculated flow behaviors for X2, in which X2 produces larger apertures during shearing than X1, thereby having a stronger conductivity.

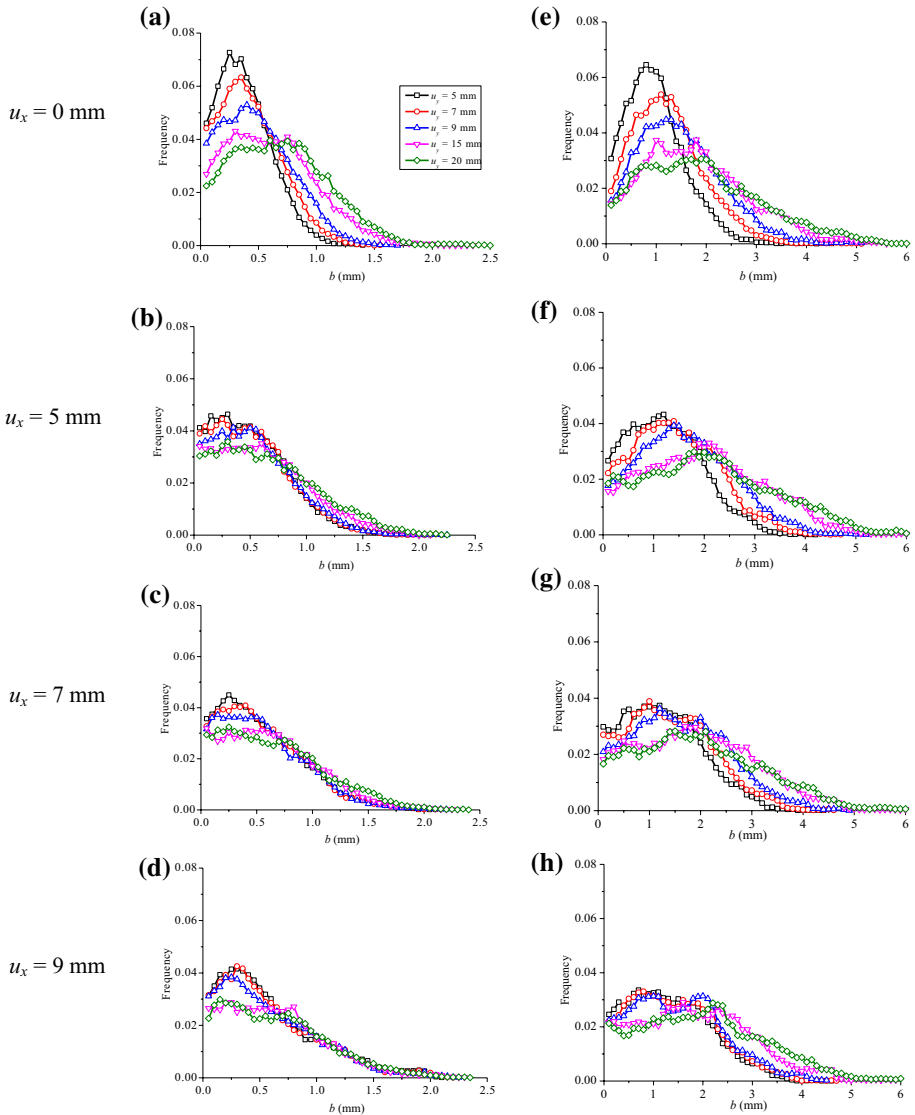


Fig. 7 Aperture-frequency curves during shearing in y direction for fracture specimens X1 **a–d** and X2 **e–h**

The evolutions of equivalent permeability in x direction (K_x), y direction (K_y), and the ratio K_x/K_y during shearing for X1 and X2 are displayed in Fig. 11. When $u_x=0$, K_x and K_y both continuously increase with increasing u_y for both X1 and X2, in which X2 generally has a larger equivalent permeability than X1. These tendencies are in consistency with the typical results obtained in previous studies (Koyama et al. 2006; Xiong et al. 2011). When there exists a historical shear displacement in x direction (i.e., $u_x \neq 0$), K_x and K_y of X1 dramatically decrease (up to almost 2 orders) due to the fracture closure induced by the change of shear direction, and then gradually increase due to the fracture dilation with

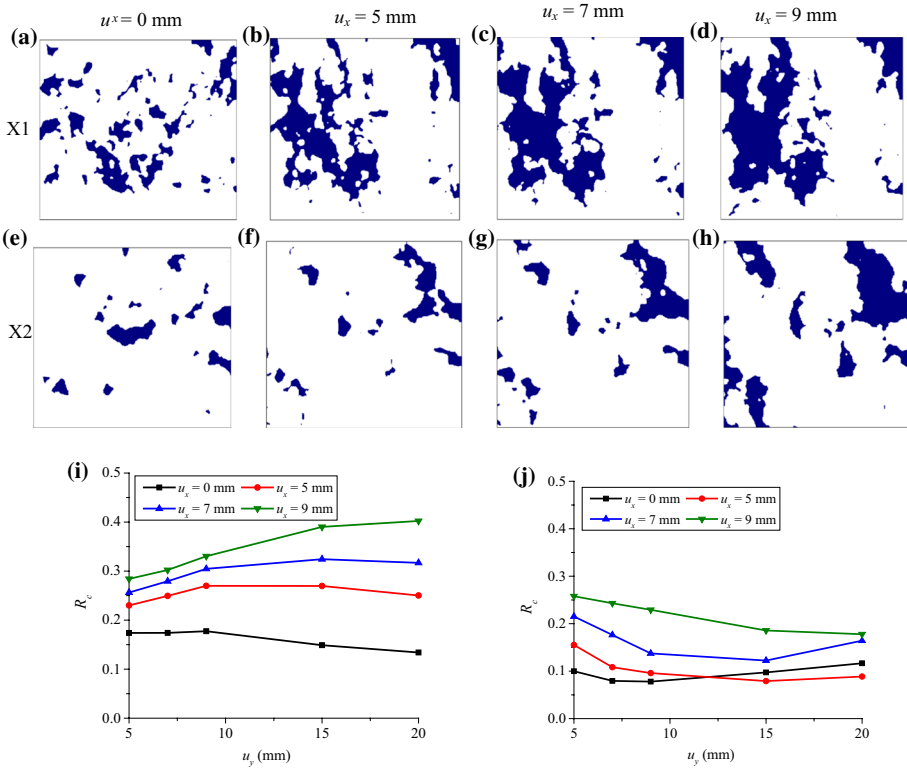


Fig. 8 Evolutions of contact areas with u_x for X1 **a–d** and X2 **e–h** at $u_y = 9$ mm, and contact ratio during shearing for **i** X1 and **f** X2

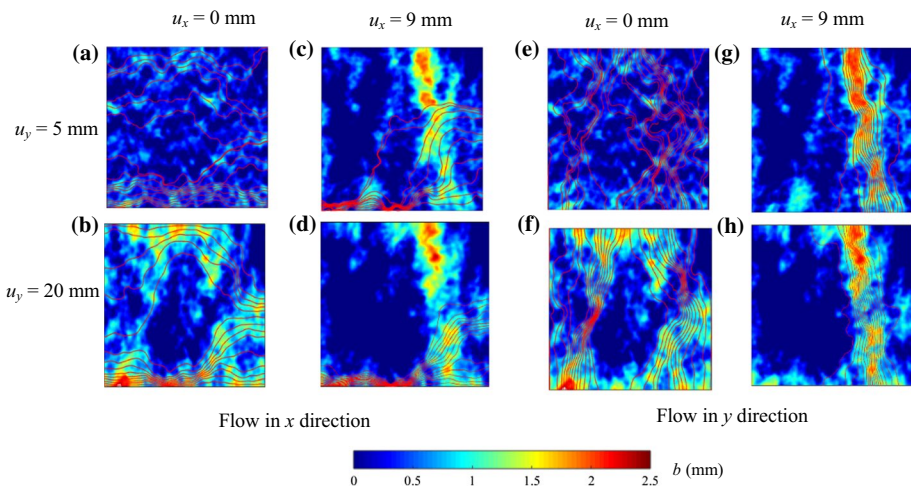


Fig. 9 Aperture distributions and main flow paths at different u_x and u_y for fracture specimen X1: **a–d** flow in x direction and **e–h** flow in y direction

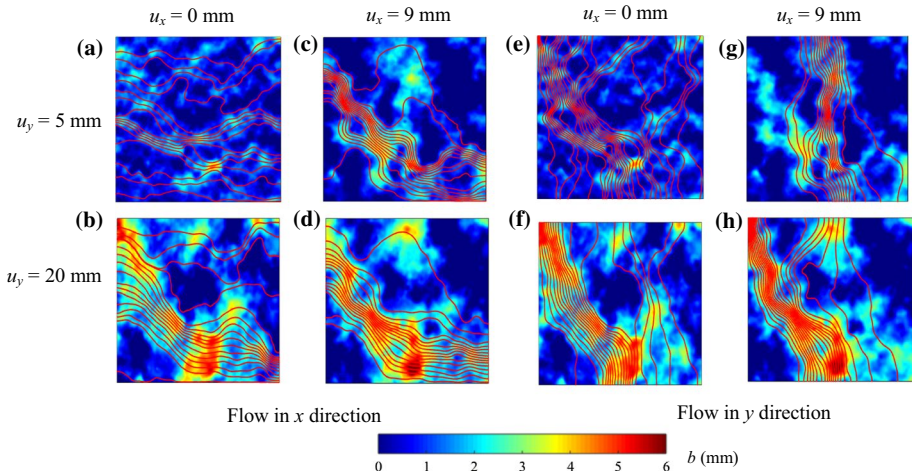


Fig. 10 Aperture distributions and main flow paths at different u_x and u_y for fracture specimen X2: **a–d** flow in x direction and **e–h** flow in y direction

increasing u_y . For X2, K_x and K_y continuously increase with increasing u_y when $u_x \leq 7$ mm. This indicates that in spite of the closure at the beginning of shearing in y direction, the overall response of X2 to shear is dilation considering the historical shear displacement in x direction. However, when $u_x = 9$ mm, K_x and K_y decrease at the beginning of shearing in y direction, caused by the more significant closure induced by the change of shear direction under a larger historical shear displacement.

The K_y/K_x keeps to be smaller than 1.0 during shearing in y direction for X1 when $u_x = 0$, indicating that the equivalent permeability in the direction parallel to shear direction is larger than that perpendicular to shear direction. However, once X1 undergoes a transition of shearing from x to y direction, K_y/K_x becomes to be larger than 1.0, due to the significant flow enhancement in y direction during historical shearing in x direction. The K_y/K_x generally decreases approaching to 1.0 with increasing u_y for both X1 and X2, expect for a slight increase at the beginning of shearing for X1.

4.3 Solute Transport Properties

The distribution of solute concentrations during shearing at different timescales for X1 and X2 is displayed in Figs. 12 and 13, respectively. The results reveal that the continuous concentration released on the inlet boundary gradually migrates along with the flow paths. For both fractures after a short time of injection, the solute firstly travels through the main flow channels and reaches the outlet boundary rapidly. The regions with small apertures that are connected to the main flow channels tend to be contaminated slowly due to low diffusion effect and flow velocity. No solute reaches to the island regions with nonzero apertures that are surrounded by contact areas. After a long time of injection, the solutes are widely distributed within the entire fracture plane with $u_x = 0$ mm. As u_x increases, the solutes become to be concentrated within limited flow channels due to large fragments of contact area caused by fracture closure. This phenomenon is especially obvious for X1 (Fig. 12e–h), in which the travel paths are restricted in the bottom of the fracture. The final distribution patterns of solute concentrations with flow in x and y directions are similar

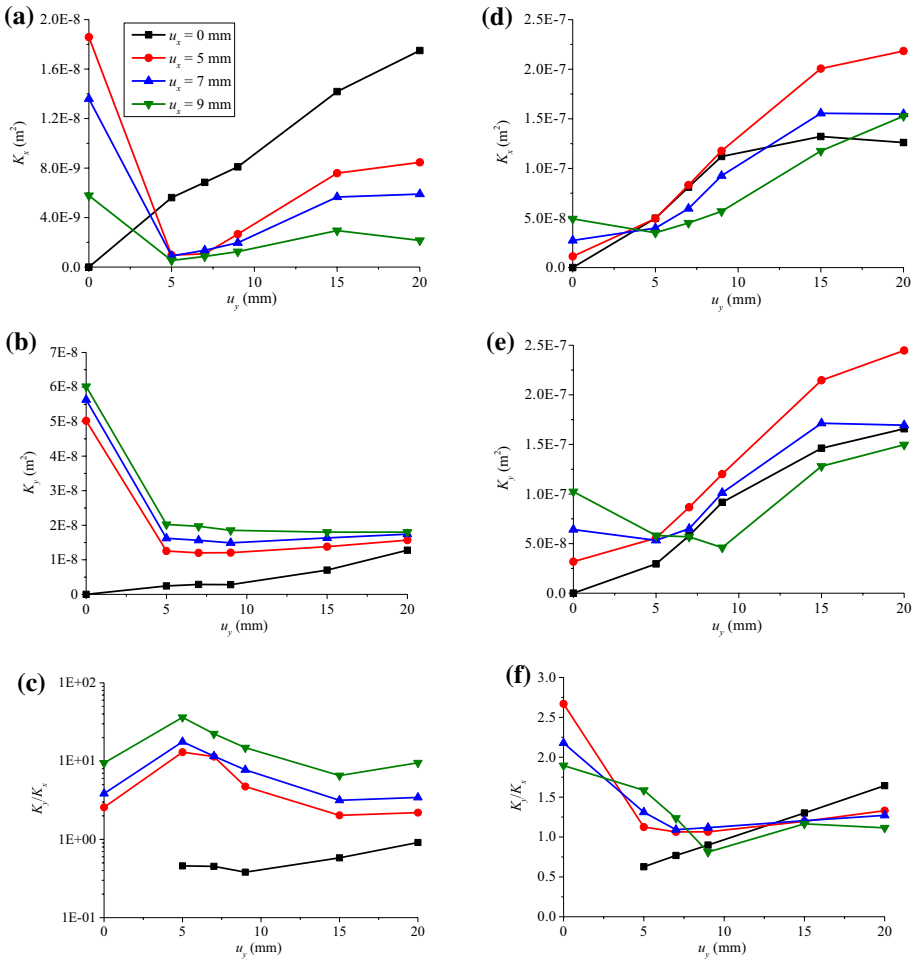


Fig. 11 Evolutions of K_x , K_y and K_y/K_x during shearing for fracture specimen X1 **a–c** and X2 **d–f**

when $u_x=0$ mm, whereas when $u_x=9$ mm, the distribution patterns are significantly different in spite of the same aperture field of the fracture. Comparing Fig. 12 with Fig. 13 shows that it takes much less time for the solute to travel through the fracture with a larger JRC under the same shear displacement. This effect can be illustrated with the aid of breakthrough curves that show the evolutions of solute concentration with time.

The breakthrough curves for the solute transport in x direction (c_x) and y direction (c_y) through X1 and X2 are displayed in Figs. 14 and 15, respectively. For both fractures, the breakthrough curves generally shift to the left as u_y increases, indicating that it takes less time for the solute to migrate through the fracture under a larger shear displacement. Under a same u_y , the breakthrough curves also tend to shift left with increasing u_x , except for the cases of X1 with flow in x direction (Fig. 14a–d), in which the breakthrough curves become more flat with a larger historical shear displacement. This is because the increasing historical shear displacement induces very limited flow paths located at the bottom of the fracture as shown in Fig. 9c–d, and the solute has to pass through the areas having

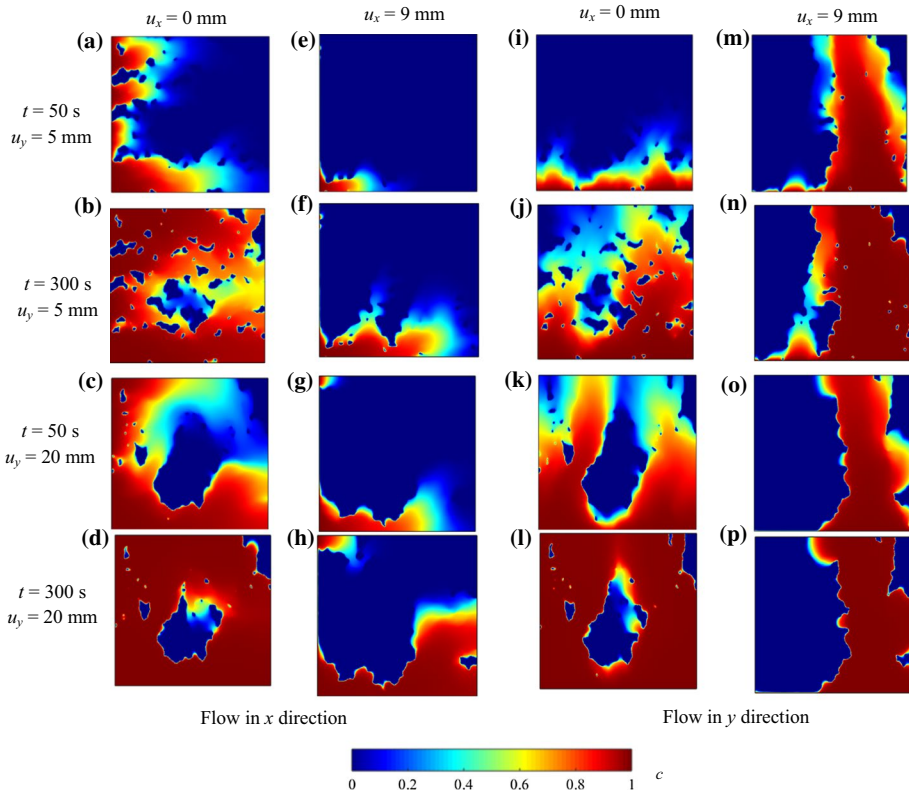


Fig. 12 Evolutions of solute concentration over time for fracture specimen X1 with the flow in different directions during shearing: **a–h** flow in x direction and **i–p** flow in y direction

low permeability to reach the outlet boundary. For some cases within the simulated time, the maximum mean concentration at the outlet boundary cannot reach the maximal concentration of 1.0 that is released on the inlet boundary. For example, the maximum mean concentration of the breakthrough curve for X1 with $u_x = 9$ mm and $u_y = 5$ mm is 0.429 and a much longer time is needed for the mean concentration at the outlet boundary to reach to 1.0. The solutes reach the outlet boundary with much less time for X2 than that for X1. As a result, the breakthrough curve of X2 becomes steep and shifts to left with respect to that of X1, implying an increase in the tracer velocity. The breakthrough curves of X1 and X2 are fitted using Eq. (9) by adjusting both the velocity and dispersivity, and the best-fitted results are presented by the dot lines in Figs. 14 and 15. For most cases, Eq. (9) is capable of capturing the shape of breakthrough curves, which indicates the transport within fractures follows Fickian dispersion. However, some fitting results are not satisfactory (e.g., Fig. 14b with $u_y = 15$ mm and 20 mm), in which the analytical solution of the Eq. (9) is unable to model the long-time tailing in breakthrough curves that characterizes the non-Fickian dispersion. This is mainly due to the high heterogeneity of the aperture distribution induced by shearing of rough-walled fractures (Bauget and Fourar 2008).

The calculated Peclet numbers using Eq. (10) for solute transport with flow in x direction (Pe_x) and y direction (Pe_y) for X1 and X2 are displayed in Fig. 16. A larger Peclet number

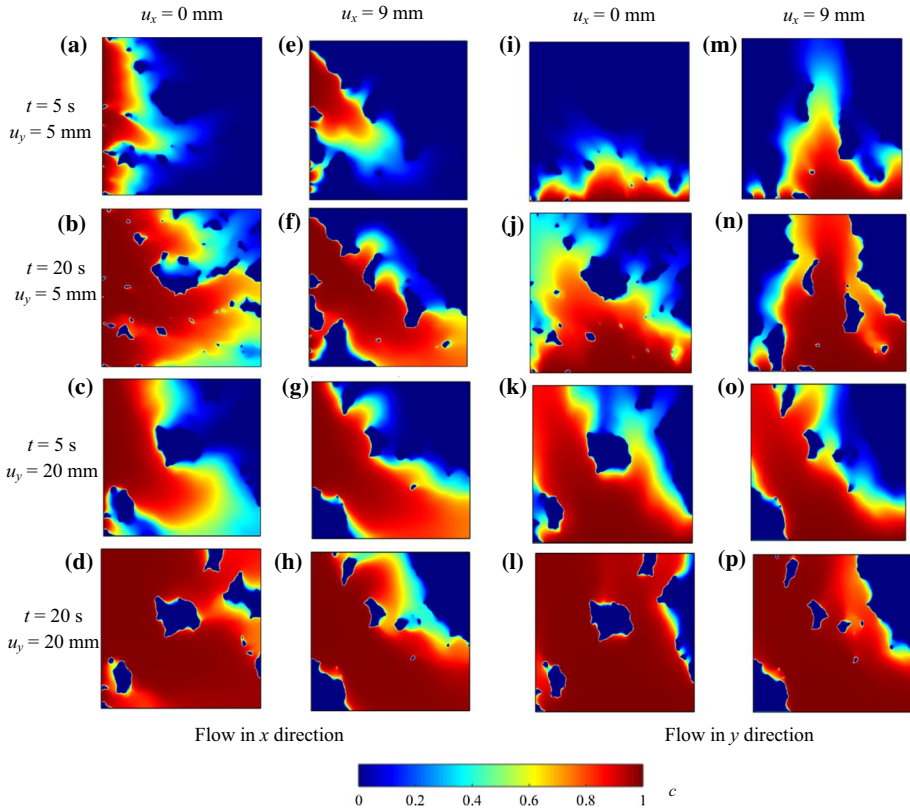


Fig. 13 Evolutions of solute concentration over time for fracture specimen X2 with the flow in different directions during shearing: **a–h** flow in x direction and **i–p** flow in y direction

means advective transport that is more dominant accompanying with a decreasing dispersivity. Both Pe_x and Pe_y generally decrease with increasing u_y in spite of the magnitude of u_x , even though some exceptions are observed. This indicates that the dispersion becomes much significant with shearing due to the increasingly concentrated contact areas and flow channels. The Pe_x changes more drastically during shearing in y direction than Pe_y , and the evaluated Peclet number in this study has the same order of magnitude with those reported in experimental and numerical tests (Koyama et al. 2008; Vilarrasa et al. 2011). For X1, Pe_x is smaller than Pe_y when $u_x=0$ during shearing in y direction, indicating that advective transport is more dominant when flow is parallel to shear direction than perpendicular to shear direction. If there exists a historical shear displacement in x direction (i.e., $u_x \neq 0$), Pe_y decreases to be smaller than Pe_x , which indicates that the dispersion in y direction is enhanced by historical shearing. The influence of the historical shear on the Peclet number of X2 is less obvious than that of X1.

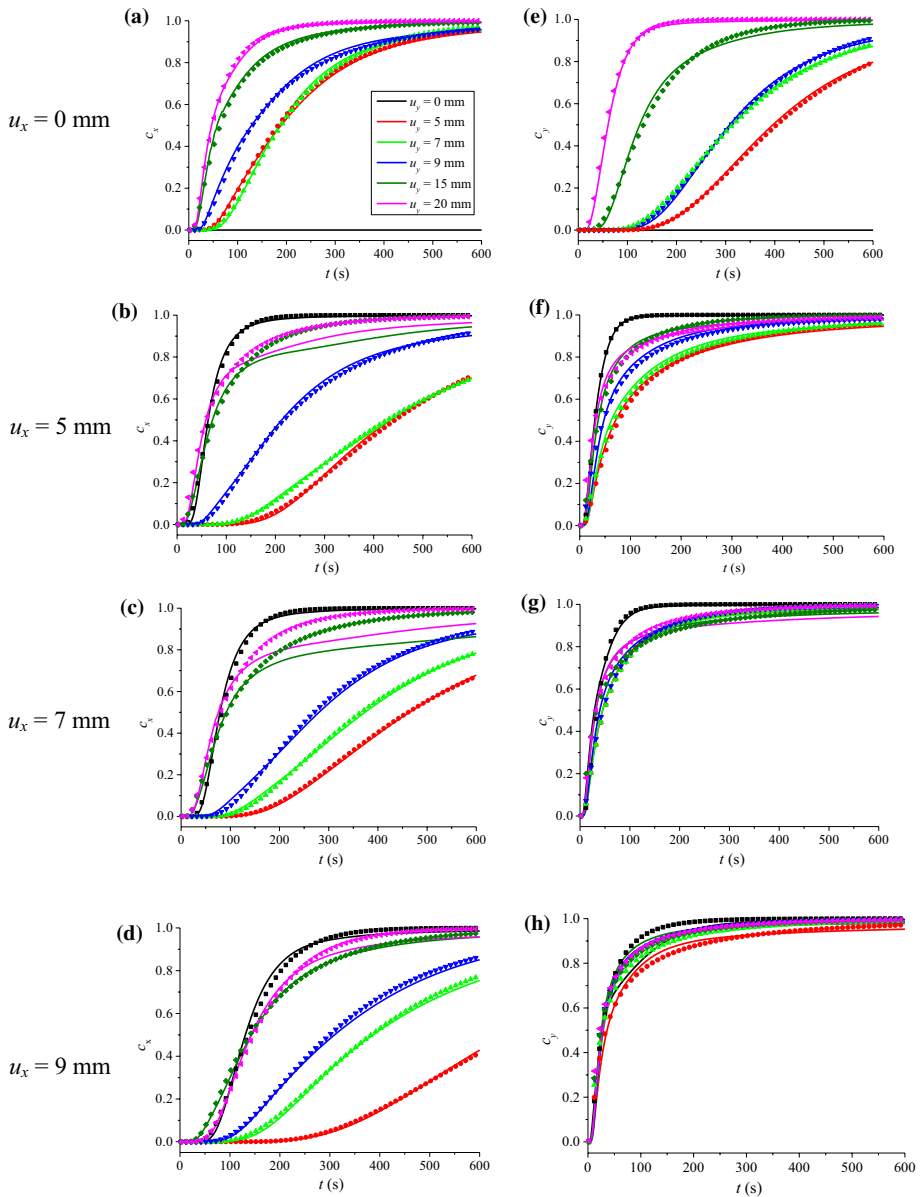


Fig. 14 Simulated breakthrough curves (the solid lines) at outlet boundary and the best-fitted results (the dot lines) using the Eq. (9) for fracture specimen X1 with the flow in different directions during shearing: **a–d** flow in *x* direction and **e–h** flow in *y* direction

5 Conclusions

In this study, a fracture model subjected to shear displacement at different directions is presented to analyze the shear-flow-transport characteristics of single rough-walled rock

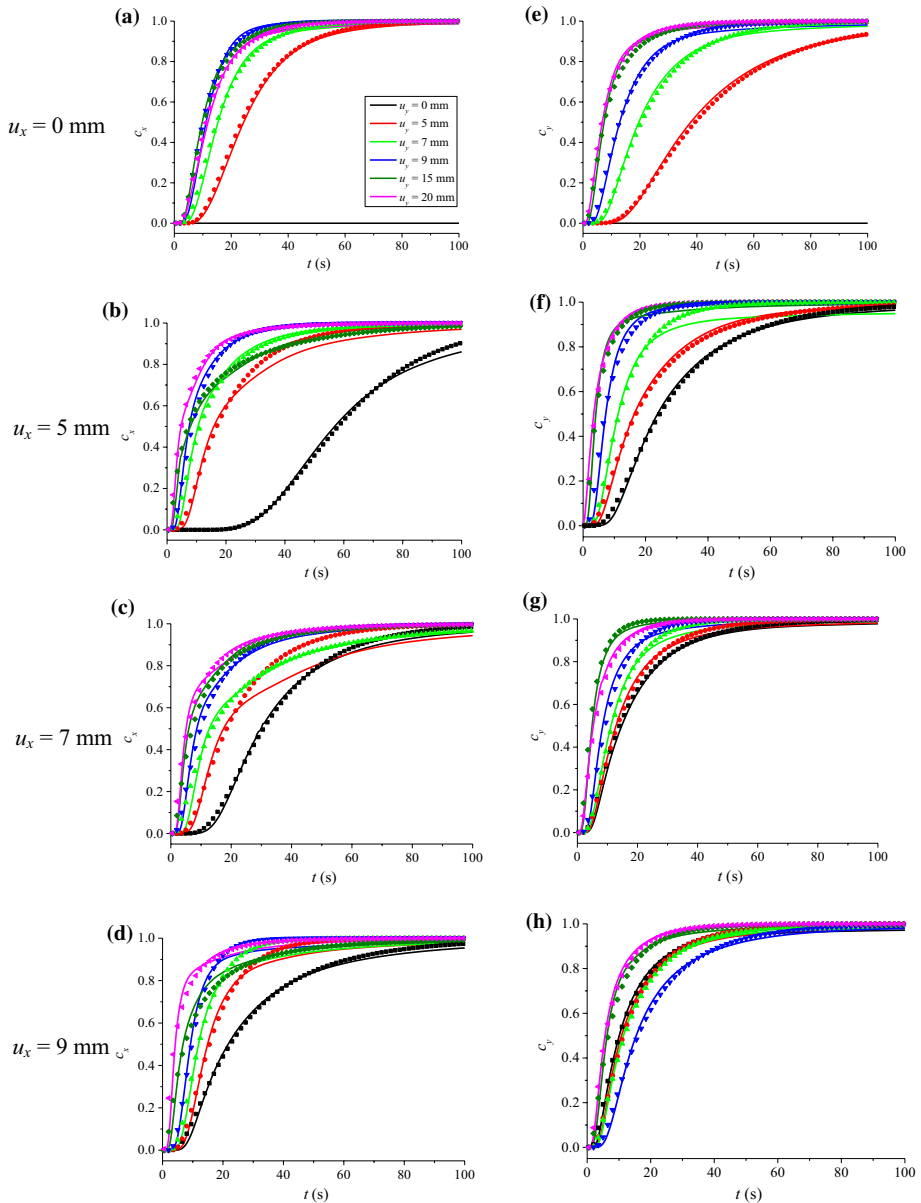


Fig. 15 Simulated breakthrough curves (the solid lines) at outlet boundary and the best-fitted results (the dot lines) using the Eq. (9) for fracture specimen X2 with the flow in different directions during shearing: **a–d** flow in x direction and **e–h** flow in y direction

fractures. Although the flow and transport processes in rock fractures during shearing have been investigated for a long time with many applications, the novelty of this study is that the effect of shear direction change on their variations was analyzed for the first time, if any. A series of shear tests on two artificial fractures with different surface roughness

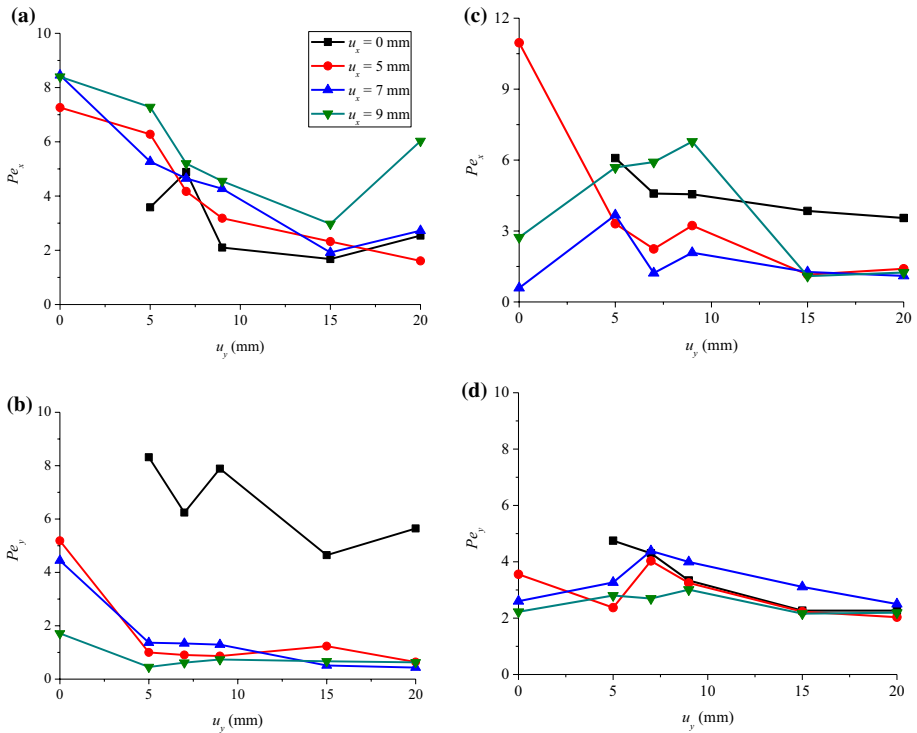


Fig. 16 Evolutions of Pe_x and Pe_y during shearing for fracture specimen X1 **a, b**, and X2 **c, d**

are conducted, in which the shear direction is altered perpendicularly during shearing. The aperture distributions during shearing with variable shear directions were estimated by analyzing the fracture asperity geometry and shear dilation measured in the laboratory tests. The calculated aperture fields were applied to simulate fluid flow and solute transport in directions parallel and perpendicular to shear direction using a finite element method code. The evolutions of flow rate, equivalent permeability, solute transport path and transport time, breakthrough curves and Pelet number during shearing with different historical shear displacements were investigated.

The results show that in the direct shear tests, the shear stress increases abruptly to a peak value and then gradually declines to a residual value with increasing shear displacement, accompanied by a continuously increasing normal displacement (i.e., dilation). When the shear direction is changed perpendicularly, the shear stress directly increases to the residual value with no obvious peak value compared to the direct shear test. The normal displacement firstly decreases (i.e., closure) to a minimum value due to void space induced by historical shearing and then changes to increase with continuously increasing shear displacement. The maximum closure increases with increasing historical shear displacement. The final normal displacement depends on the competition between the dilation and closure induced by the shear in two directions, which directly determines the aperture distribution thereby affecting the flow and transport processes through fractures. The fracture closes more significantly for the fracture with a smaller JRC, resulting in a more significant decrease (up to almost 2 orders) in equivalent permeability when changing the

shear direction perpendicularly. The ratio of the permeability in the direction parallel to shear direction to that perpendicular to shear direction is usually smaller than 1.0 in the direct shear test. However, when the shear direction is changed perpendicularly, this ratio changes to be larger than 1.0 due to the significant flow channeling in direction parallel to shear induced by historical shearing. The solute migrates through the fast flow channels and the low-permeability areas to reach the outlet boundary. The historical shear can either promote or block the solute transport depending on the distributions of void spaces and contact obstacles induced by shearing in two directions. The Peclet number generally decreases with increasing shear displacement in spite of the magnitude of historical shear displacement, which indicates that the dispersion becomes more dominant than advection due to the increasingly concentrated contact areas and flow channels with shearing.

The shear tests were conducted under a relatively small normal stress of 1.0 MPa to avoid damage on the fracture asperities; however, slight surface damages have been observed by comparing the fracture surface before and after the shear tests, which may affect the flow and transport behaviors through fractures (Zhao et al. 2018). The destruction of asperities was not taken into account when generating the numerical models. We adopted these simple models for establishing useful experimental and numerical approaches, and demonstrated the importance of shear direction change for continued fundamental researches. In the future, we will investigate the characteristics of the asperity degradation during shearing in different directions, and quantify their effects on the coupled shear-flow-transport processes in rock fractures. Besides, the application in this study is limited to the fractures at the laboratory scale. It cannot be directly extended to large fractures since previous studies have shown that the hydro-mechanical properties of rock fractures are commonly scale dependent (Koyama et al. 2006; Matsuki et al. 2006). However, the scale effect is an important issue and its influence on the coupled shear-flow-transport properties of rock fractures should be studied in future works.

Acknowledgements This study has been partially funded by Natural Science Foundation of China, China (Grant Nos. 51734009, 51709260 and 51909269), China Postdoctoral Science Foundation National (2019M652506) and Natural Science Foundation of Jiangsu Province, China (No. BK20170276). These supports are gratefully acknowledged.

References

- Auradou, H., Drazer, G., Boschan, A., Hulin, J.P., Koplik, J.: Flow channeling in a single fracture induced by shear displacement. *Geothermics* **35**(5–6), 576–588 (2006)
- Bauget, F., Fourar, M.: Non-Fickian dispersion in a single fracture. *J. Contam. Hydrol.* **100**(3–4), 137–148 (2008)
- Barbier, E.: Geothermal energy technology and current status: an overview. *Renew. Sustain. Energy Rev.* **6**(1–2), 3–65 (2002)
- Bear, J.: *Dynamics of Fluids in Porous Media*. Elsevier, New York (1972)
- Boutt, D.F., Grasselli, G., Fredrich, J.T., Cook, B.K., Williams, J.R.: Trapping zones: the effect of fracture roughness on the directional anisotropy of fluid flow and colloid transport in a single fracture. *Geophys. Res. Lett.* **33**(21) (2006)
- Brown, S.R.: Fluid flow through rock joints: the effect of surface roughness. *J. Geophys. Res.* **92**(B2), 1337–1347 (1987)
- Brown, S.R., Stockman, H.W., Reeves, S.J.: Applicability of the Reynolds equation for modeling fluid flow between rough surfaces. *Geophys. Res. Lett.* **22**(18), 2537–2540 (1995)
- Cheng, L., Rong, G., Yang, J., Zhou, C.: Fluid flow through single fractures with directional shear dislocations. *Transp. Porous Media* **118**(2), 301–326 (2017)
- Chern, S.G., Cheng, T.C., Chen, W.Y.: Behavior of regular triangular joints under cyclic shearing. *J. Mar. Sci. Technol.* **20**(5), 508–513 (2012)

- Crandall, D., Bromhal, G., Karpyn, Z.T.: Numerical simulations examining the relationship between wall-roughness and fluid flow in rock fractures. *Int. J. Rock Mech. Min. Sci.* **47**(5), 784–796 (2010)
- de Dreuzy J. R., Méheust Y., Pichot G. Influence of fracture scale heterogeneity on the flow properties of three-dimensional discrete fracture networks (DFN). *J. Geophys. Res.* **117**(B11) (2012)
- de Marsily, G.: *Quantitative Hydrogeology*, pp. 266–270. Academic Press, San Diego (1986)
- Fardin, N.: *The Effect of Scale on the Morphology, Mechanics and Transmissivity of Single Rock Fractures*. Mark och vatten, Stockholm (2003)
- Huang, N., Liu, R., Jiang, Y.: Numerical study of the geometrical and hydraulic characteristics of 3D self-affine rough fractures during shear. *J. Nat. Gas Sci. Eng.* **45**, 127–142 (2017)
- Huang, N., Jiang, Y., Liu, R., Xia, Y.: Size effect on the permeability and shear induced flow anisotropy of fractal rock fractures. *Fractals* **26**(02), 1840001 (2018)
- Huang, N., Liu, R., Jiang, Y., Cheng, Y., Li, B.: Shear-flow coupling characteristics of a three-dimensional discrete fracture network-fault model considering stress-induced aperture variations. *J. Hydrol.* **571**, 416–424 (2019)
- Hudson, J.A.: Understanding of measured changes in rock structure, in situ stress and water flow caused by underground excavation. In: *Proc 2nd International Symposium on Field Measurements in Geomechanics*, Kobe, 6–9 April 1987 V2, P605-612. Publ Rotterdam: AA Balkema, 1988[C]/*International Journal of Rock Mechanics and Mining Sciences & Geomechanics Abstracts*. Pergamon, vol. 27(2), p. A119 (1990)
- Hutson, R.W., Dowding, C.H.: Joint asperity degradation during cyclic shear. *Int. J. Rock Mech. Min. Sci. Geomech. Abstracts* **27**(2), 109–119 (1990)
- Indraratna, B., Thirukumar, S., Brown, E.T., Zhu, S.P.: Modelling the shear behaviour of rock joints with asperity damage under constant normal stiffness. *Rock Mech. Rock Eng.* **48**(1), 179–195 (2015)
- Javadi, M., Sharifzadeh, M., Shahriar, K., Mitani, Y.: Critical Reynolds number for nonlinear flow through rough-walled fractures: the role of shear processes. *Water Resour. Res.* **50**(2), 1789–1804 (2014)
- Jiang, Y., Tanabashi, Y., Xiao, J.: An improved shear-flow test apparatus and its application to deep underground construction. *Int. J. Rock Mech. Min. Sci.* **41**, 170–175 (2004a)
- Jiang, Y., Xiao, J., Tanabashi, Y., Mizokami, T.: Development of an automated servo-controlled direct shear apparatus applying a constant normal stiffness condition. *Int. J. Rock Mech. Min. Sci.* **41**(2), 275–286 (2004b)
- Jiang, Y., Li, B., Tanabashi, Y.: Estimating the relation between surface roughness and mechanical properties of rock joints. *Int. J. Rock Mech. Min. Sci.* **43**(6), 837–846 (2006)
- Koyama, T., Li, B., Jiang, Y., Jing, L.: Numerical simulations for the effects of normal loading on particle transport in rock fractures during shear. *Int. J. Rock Mech. Min. Sci.* **45**(8), 1403–1419 (2008)
- Koyama, T., Fardin, N., Jing, L., Stephansson, O.: Numerical simulation of shear-induced flow anisotropy and scale-dependent aperture and transmissivity evolution of rock fracture replicas. *Int. J. Rock Mech. Min. Sci.* **43**(1), 89–106 (2006)
- Lanaro, F.: A random field model for surface roughness and aperture of rock fractures. *Int. J. Rock Mech. Min. Sci.* **37**(8), 1195–1210 (2000)
- Lee, H.S., Cho, T.F.: Hydraulic characteristics of rough fractures in linear flow under normal and shear load. *Rock Mech. Rock Eng.* **35**(4), 299–318 (2002)
- Li, B., Jiang, Y., Koyama, T., et al.: Experimental study of the hydro-mechanical behavior of rock joints using a parallel-plate model containing contact areas and artificial fractures. *Int. J. Rock Mech. Min. Sci.* **45**(3), 362–375 (2008)
- Liu, R., Huang, N., Jiang, Y., Jing, H., Li, B., Xia, Y.: Effect of shear displacement on the directivity of permeability in 3D self-affine fractal fractures. *Geofluids*, 9813846 (2018a)
- Liu, R., Jiang, Y., Huang, N., Sugimoto, S.: Hydraulic properties of 3D crossed rock fractures by considering anisotropic aperture distributions. *Adv. Geo-Energy Res.* **2**(2), 113–121 (2018b)
- Li, Y., Sun, S.: Analytical prediction of the shear behaviour of rock joints with quantified waviness and unevenness through wavelet analysis. *Rock Mech. Rock Eng.* (2019). <https://doi.org/10.1007/s00603-019-01817-5>
- Matsuki, K., Chida, Y., Sakaguchi, K., Glover, P.W.J.: Size effect on aperture and permeability of a fracture as estimated in large synthetic fractures. *Int. J. Rock Mech. Min. Sci.* **43**(5), 726–755 (2006)
- Matsuki, K., Kimura, Y., Sakaguchi, K., Kizaki, A., Giwelli, A.A.: Effect of shear displacement on the hydraulic conductivity of a fracture. *Int. J. Rock Mech. Min. Sci.* **47**(3), 436–449 (2010)
- Neretnieks, I.: Diffusion in the rock matrix: an important factor in radionuclide retardation? *J. Geophys. Res.* **85**(B8), 4379–4397 (1980)
- Olsson, R., Barton, N.: An improved model for hydromechanical coupling during shearing of rock joints. *Int. J. Rock Mech. Min. Sci.* **38**(3), 317–329 (2001)

- Rahman, M.K., Hossain, M.M., Rahman, S.S.: A shear-dilation-based model for evaluation of hydraulically stimulated naturally fractured reservoirs. *Int. J. Numer. Anal. Methods Geomech.* **26**(5), 469–497 (2002)
- Raven, K.G., Gale, J.E.: Water flow in a natural rock fracture as a function of stress and sample size. *Int. J. Rock Mech. Min. Sci. Geomech. Abstracts Pergamon* **22**(4), 251–261 (1985)
- Rong, G., Yang, J., Cheng, L., Zhou, C.: Laboratory investigation of nonlinear flow characteristics in rough fractures during shear process. *J. Hydrol.* **541**, 1385–1394 (2016)
- Sun, J., Zhao, Z.: Effects of anisotropic permeability of fractured rock masses on underground oil storage caverns. *Tunn. Undergr. Space Technol.* **25**(5), 629–637 (2010)
- Thompson, M.E.: Numerical simulation of solute transport in rough fractures. *J. Geophys. Res.* **96**(B3), 4157–4166 (1991)
- Thompson, M.E., Brown, S.R.: The effect of anisotropic surface roughness on flow and transport in fractures. *J. Geophys. Res.* **96**(B13), 21923–21932 (1991)
- Tsang, Y.W., Witherspoon, P.A.: The dependence of fracture mechanical and fluid flow properties on fracture roughness and sample size. *J. Geophys. Res.* **88**(B3), 2359–2366 (1983)
- Vilarraza, V., Koyama, T., Neretnieks, I., Jing, L.: Shear-induced flow channels in a single rock fracture and their effect on solute transport. *Transp. Porous Media* **87**(2), 503–523 (2011)
- Wang, M., Chen, Y.F., Ma, G.W., Zhou, J.Q., Zhou, C.B.: Influence of surface roughness on nonlinear flow behaviors in 3D self-affine rough fractures: lattice Boltzmann simulations. *Adv. Water Resour.* **96**, 373–388 (2016)
- Wang, J., Zhou, Z.: Simulation on solute transport in fractured rocks based on fractal theory. *Chin. J. Rock Mech. Eng.* **23**(8), 1358–1362 (2004)
- Watanabe, N., Hirano, N., Tsuchiya, N.: Diversity of channeling flow in heterogeneous aperture distribution inferred from integrated experimental-numerical analysis on flow through shear fracture in granite. *J. Geophys. Res.* **114**(B4) (2009)
- Witherspoon, P.A., Wang, J.S.Y., Iwai, K., Gale, J.E.: Validity of cubic law for fluid flow in a deformable rock fracture. *Water Resour. Res.* **16**(6), 1016–1024 (1980)
- Wu, X., Jiang, Y., Gong, B., Guan, Z., Deng, T.: Shear performance of rock joint reinforced by fully encapsulated rock bolt under cyclic loading condition. *Rock Mech. Rock Eng.* 1–10 (2018)
- Xiong, X., Li, B., Jiang, Y., Koyama, T., Zhang, C.: Experimental and numerical study of the geometrical and hydraulic characteristics of a single rock fracture during shear. *Int. J. Rock Mech. Min. Sci.* **48**(8), 1292–1302 (2011)
- Zhang, X., Sanderson, D.J.: Evaluation of instability in fractured rock masses using numerical analysis methods: effects of fracture geometry and loading direction. *J. Geophys. Res.* **106**(B11), 26671–26687 (2001)
- Zhao, Z., Jing, L., Neretnieks, I., Moreno, L.: Numerical modeling of stress effects on solute transport in fractured rocks. *Comput. Geotech.* **38**(2), 113–126 (2011)
- Zhao, Z., Peng, H., Wu, W., Chen, Y.F.: Characteristics of shear-induced asperity degradation of rock fractures and implications for solute retardation. *Int. J. Rock Mech. Min. Sci.* **105**, 53–61 (2018)
- Zhou, J.Q., Wang, M., Wang, L., Chen, Y.F., Zhou, C.B.: Emergence of nonlinear laminar flow in fractures during shear. *Rock Mech. Rock Eng.* **51**(11), 3635–3643 (2018)
- Zimmerman, R.W., Bodvarsson, G.S.: Hydraulic conductivity of rock fractures. *Transp. Porous Media* **23**(1), 1–30 (1996)
- Zou, L., Jing, L., Cvetkovic, V.: Roughness decomposition and nonlinear fluid flow in a single rock fracture. *Int. J. Rock Mech. Min. Sci.* **75**, 102–118 (2015)